

VALIDATION AND IMPROVEMENT OF THE PAN-STARRS PHOTOMETRIC CALIBRATION WITH THE STELLAR COLOR REGRESSION METHOD

KAI XIAO¹ HAIBO YUAN¹

Received: 2021 December 28; Revised: 2022 February 08; Accepted: 2022 February 09

ABSTRACT

As one of the best ground-based photometric dataset, Pan-STARRS1 (PS1) has been widely used as the reference to calibrate other surveys. In this work, we present an independent validation and recalibration of the PS1 photometry using spectroscopic data from the LAMOST DR7 and photometric data from the corrected Gaia EDR3 with the Stellar Color Regression (SCR) method. Using per band typically a total of 1.5 million LAMOST-PS1-Gaia stars as standards, we show that the PS1 photometric calibration precisions in the *grizy* filters are around 4 ~ 5 mmag when averaged over 20' regions. However, significant large- and small-scale spatial variation of magnitude offset, up to over 1 per cent, probably caused by the calibration errors in the PS1, are found for all the *grizy* filters. The calibration errors in different filters are un-correlated, and are slightly larger for the *g* and *y* filters. We also detect moderate magnitude-dependent errors (0.005, 0.005, 0.005, 0.004, 0.003 mag per magnitude in the 14 – 17 magnitude range for the *grizy* filters, respectively) in the PS1 photometry by comparing with the Gaia EDR3 and other catalogs. The errors are likely caused by the systematic uncertainties in the PSF magnitudes. We provide two-dimensional maps to correct for such magnitude offsets in the LAMOST footprint at different spatial resolutions from 20' to 160'. The results demonstrate the power of the SCR method in improving the calibration precision of wide-field surveys when combined with the LAMOST spectroscopy and Gaia photometry.

Subject headings: Astronomy data analysis, Stellar photometry, Calibration

1. INTRODUCTION

The current and next-generation wide-field imaging surveys such as the Sloan Digital Sky Survey (SDSS; York et al. 2000), the Panoramic Survey Telescope and Rapid Response System (Pan-STARRS; Kaiser et al. 2002), the Dark Energy Survey (DES; Flaugher et al. 2015; Dark Energy Survey Collaboration et al. 2016; Abbott et al. 2018), the Javalambre Physics of the Accelerating Universe Astrophysical Survey (J-PAS; Benitez et al. 2014), the Wide Field Survey Telescope (WFST; Lou et al. 2016), the Chinese Space Station Telescope (CSST; Zhan 2018), the Legacy Survey of Space and Time (LSST; Ivezić et al. 2019) and the Multi-channel Photometric Survey Telescope (Mephisto; Er et al. 2021, in preparation), are vital in modern astronomy in discovering and characterizing new objects and phenomena. While uniform and accurate photometric calibration play a central role in the wide-field surveys.

Recently, some new approaches have been developed for the high-precision calibration of wide field surveys. The methods can be divided into categories of either: “hardware-driven” or “software-driven” (Huang & Yuan 2022). Approaches of the former category are based on better understanding of the wide-field imaging observations, and include such as the Ubercalibration method (Padmanabhan et al. 2008), the Forward Global Calibration Method (FGCM; Burke et al. 2018), and the Hypercalibration method (Finkbeiner et al. 2016); while those of the latter category are based on better understanding of stellar colors, such as the Stellar Locus Regres-

sion method (SLR; High et al. 2009), the Stellar Locus method (SL; López-Sanjuan et al. 2019), and the Stellar Color Regression method (SCR; Yuan et al. 2015).

Owing to the rapid development of multi-fiber spectroscopic surveys, e.g., LAMOST (Deng et al. 2012; Liu et al. 2014), we have entered into the era of millions of stellar spectra. In addition, with the modern template-matching and data-driven based stellar parameter pipelines (e.g., Lee et al. 2008a,b; Wu et al. 2011; Xiang et al. 2015, 2017), stellar atmospheric parameters, such as T_{eff} , $\log g$, $[\text{Fe}/\text{H}]$, can be determined to a very high internal precision (e.g., Niu et al. 2021a). As a result, stellar colors can now be accurately predicted based on the large-scale spectroscopic surveys. Using millions of spectroscopically observed stars as color standards, Yuan et al. (2015) first proposed the spectroscopy-based SCR method and performed precise color (re-)calibrations for the SDSS Stripe 82. Compared to the other “software-driven” methods, the SCR method fully accounts the effects of metallicity, surface gravity, and dust reddening on stellar colors. When applied to the SDSS Stripe 82 (Ivezić et al. 2007), it achieved a precision of 2 – 5 mmag in the SDSS colors. The method has also been applied to the Gaia Data Release 2 and Early Data Release 3 (EDR3) to correct for the magnitude/color-dependent systematic errors in the Gaia colors (Niu et al. 2021a,b), achieving an unprecedented precision of 1 mmag. Together with the high-precision photometry from Gaia, the SCR method can further be used to predict stellar magnitudes accurately and perform photometric calibration. For example, Huang et al. (2021) have applied the method to recalibrate the DR2 of the SkyMapper Southern Survey (SMSS; Wolf et al. 2018), and find large zero-point offsets in the *uv* bands. Huang

¹ Department of Astronomy, Beijing Normal University, Beijing, 100875, People’s Republic of China; email: yuanhb@bnu.edu.cn

& Yuan (2022) have applied the method to the SDSS Stripe82 standard stars catalogs (Ivezić et al. 2007; Thanjavur et al. 2021), achieving a precision of 5 mmag in the u band, and 2 mmag in the $griz$ bands. Possible implementations of the SCR method under different situations and improvements are also discussed by Huang & Yuan (2022).

As the first part of the Pan-STARRS (Kaiser et al. 2002, 2010), Pan-STARRS1 (PS1; Tonry et al. 2012) has imaged three quarters of the sky repeatedly in five broadband filters (g, r, i, z, y). Taking advantage of the large amount of over-lapping observations, PS1 photometry has been calibrated using the ubercalibration method to a precision better than 1 per cent (Schlafly et al. 2012; Magnier et al. 2020). As one of the best ground-based photometric dataset, PS1 has been widely used as reference to calibrate other surveys, including the SDSS survey (Finkbeiner et al. 2016), the Beijing–Arizona Sky Survey (BASS; Zou et al. 2017; Zhou et al. 2018), the J-PLUS (López-Sanjuan et al. 2019, 2021). It has also been used as cross-calibration of multiple photometric systems to improve the cosmological measurements with Type Ia supernovae (see Scolnic et al. 2015; Brout et al. 2021).

In this work, using the SCR method with the corrected photometric data from the Gaia EDR3 (Yang et al. 2021) and the spectroscopic data from LAMOST DR7, validation and improvement of the PS1 photometric calibration are performed. The paper is organized as follows. In Sections 2 and 3, we introduce the data used and the validation process with the SCR method in this work. The results are presented in Section 4 and discussed in Section 5. Conclusions are given in Section 6.

2. DATA

2.1. Pan-STARRS 1 Data Release 1

The PS1 survey has imaged three quarters of the sky in five broadband filters (g, r, i, z, y), using its 1.8 meter telescope of a 3.3° field of view (Hodapp et al. 2004) and 1.4 Gigapixel camera. Its first public data release (DR1) on 16 December 2016 contains the results of the third full reduction of the Pan-STARRS 3π Survey (Magnier et al. 2020). The typical 5σ limiting magnitudes for point sources are (23.3, 23.2, 23.1, 22.3, 21.4) in the (g, r, i, z, y) bands, respectively (Chambers et al. 2016). PSF magnitudes, Kron magnitudes, and aperture magnitudes are provided in the PS1 DR1. PSF magnitudes are obtained from fitting a predefined PSF model using maximum-likelihood methods, and mainly for stars. Kron magnitudes are mainly for extended sources. Aperture magnitudes measure the total flux for a point source based on integration over an aperture plus an extrapolation according to the PSF. In this work, PSF magnitudes are used as default.

2.2. Gaia Early Data Release 3

The EDR3 (Gaia Collaboration et al. 2021a,b) of the European Space Agency (ESA)’s space mission Gaia (Gaia Collaboration et al. 2016) has delivered not only the best astrometric information but also the best photometric data for about 1.8 billion stars in G, G_{BP} and G_{RP} bands, in terms of full sky coverage, uniform calibration at mmag level, and small photometric errors for

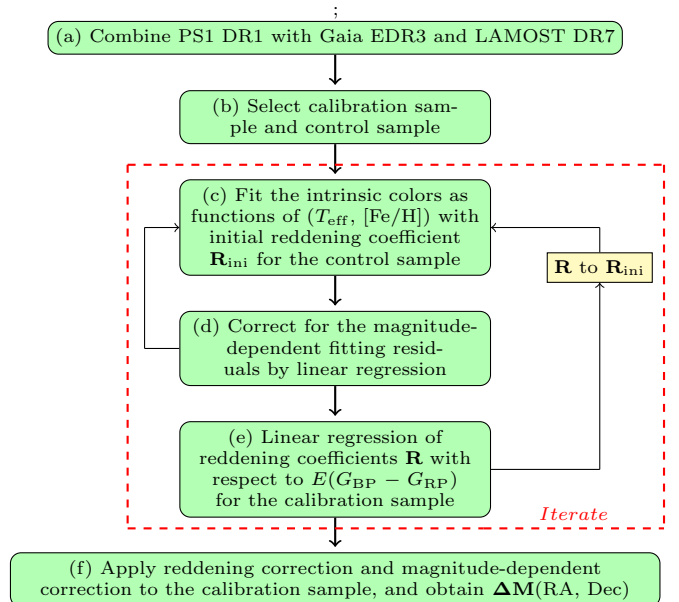


FIG. 1.— Flowchart of the SCR method in this work for a given PS1 passband.

a very wide range of magnitudes. The overall calibration errors are less than 1 mmag for overall trend except for very blue and bright sources (Riello et al. 2021). More recently, Yang et al. (2021) carried out an independent validation of Gaia EDR3 photometry against about 10,000 Landolt standard stars using a machine-learning technique. They obtained magnitude-dependent corrections up to 10 mmag for the three Gaia bands. Hence, Gaia EDR3 magnitudes hereafter refer to those corrected by Yang et al. (2021).

2.3. LAMOST Data Release 7

The Large Sky Area Multi-Object Fiber Spectroscopic Telescope (LAMOST; Cui et al. 2012; Zhao et al. 2012; Deng et al. 2012; Liu et al. 2014) is a quasi-meridian reflecting Schmidt telescope with 4000 fibers, and has a field of view of 20 deg^2 . Its Data Release 7 (hereafter DR7; see Luo et al. 2015) includes a total number of 10,640,255 low resolution spectra covering the whole optical wavelength range of 369 – 910 nm at a spectral resolution of about 1800. The LAMOST Stellar Parameter Pipeline (LASP; Wu et al. 2011) has been used to determine the basic stellar parameters including effective temperature T_{eff} , surface gravity $\log g$ and metallicity $[\text{Fe}/\text{H}]$. The typical precision is about 110 K for T_{eff} , 0.2 dex for $\log g$, and 0.1 dex for $[\text{Fe}/\text{H}]$ (Luo et al. 2015).

3. VALIDATION PROCESS WITH THE SCR METHOD

An overview of the validation process using the SCR method to the PS1 calibration is shown in Figure 1. The details are as below:

- Combine the PS1 DR1 photometric data with the Gaia EDR3 and the LAMOST DR7. The adopted cross-matching radius is $1''$.
- Select main sequence stars ($\log g > -3.4 \times 10^{-4} \times T_{\text{eff}} + 5.8$) as the calibration samples with the following constraints: 1) $\text{mag}\{g, r, i, z\}$

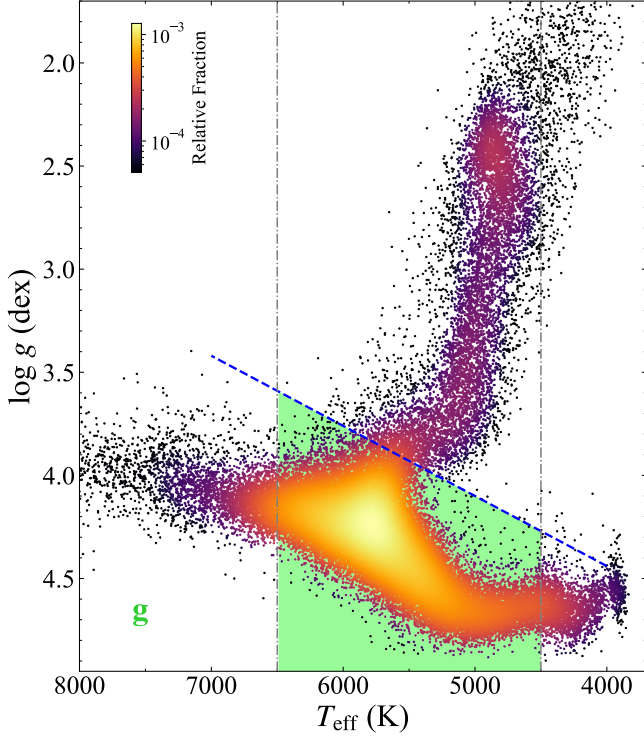


FIG. 2.— Distribution of stars in the $T_{\text{eff}}\text{-log } g$ plane for the g band. Calibration sample stars are distributed in the green-background region. The two vertical dotted lines mark $T_{\text{eff}} = 6500$ K and 4500 K. The blue dotted line marks the boundary between the main-sequence and giant stars. A color bar at the upper-left corner indicating the normalized stellar densities.

> 14 and $\text{mag}\{y\} > 13$ to avoid saturation; 2) $\text{error}\{g, r, i, z, y\} < 0.02$ mag; 3) $\text{phot_bp_rp_excess_factor} < 1.3 + 0.06 \times (G_{\text{BP}} - G_{\text{RP}})^2$ to avoid bad Gaia photometry; 4) $4500 < T_{\text{eff}} < 6500$ K, a relatively narrow temperature range for robust fitting of intrinsic colors with atmospheric parameters and the temperature-dependence reddening coefficients, but still with sufficient numbers of stars; 5) $[\text{Fe}/\text{H}] > -1$ for an easy intrinsic color fitting with atmospheric parameters; and 6) Signal-to-noise ratio for the g band (SNR_g) of the LAMOST spectra > 20 . Finally, 1,688,097, 1,299,006, 1,162,825, 1,113,294 and 1,931,225 stars are selected in the g, r, i, z and y bands, respectively. The calibration sample in the g band is shown in Figure 2 and 3. Then, the control sample stars are selected as those within a small and low-extinction area ($153 < \text{RA} < 159$ degree, $40 < \text{Dec} < 46$ degree). A total number of 2844, 2256, 2139, 2084 and 3389 control stars are selected for the $grizy$ bands, respectively. Their spatial distributions are shown in Figure 4.

For reddening correction, the dust reddening map of Schlegel et al. (1998) is not used as it fails at low Galactic latitudes and shows spatially-dependent systematic errors (Sun et al., submitted). In this work, the values of $E(G_{\text{BP}} - G_{\text{RP}})$ obtained with the star-pair method (Yuan et al. 2013; Ruoyi & Haibo 2020) are adopted instead.

c. Five colors $\mathbf{C} = \mathbf{G}_{\text{BP,RP}} - \mathbf{M}^{\text{obs}}$ are

adopted for the *grizy* bands, where $\mathbf{G}_{\text{BP,RP}} = (G_{\text{BP}}, G_{\text{RP}}, G_{\text{RP}}, G_{\text{RP}}, G_{\text{RP}})^{\text{T}}$ and $\mathbf{M}^{\text{obs}} = (g, r, i, z, y)^{\text{T}}$. Then, for the control sample, a 2nd-order two-dimensional polynomial (with 6 free parameters, see Equation (1)) as a function of T_{eff} and $[\text{Fe}/\text{H}]$ is used to fit the intrinsic colors (\mathbf{C}_0). Here the intrinsic colors are estimated using Equation (2), where \mathbf{R} represents reddening coefficients.

$$\begin{aligned} \mathbf{C}_0^{\text{mod}} = & \mathbf{a}_0 \cdot T_{\text{eff}}^2 + \mathbf{a}_1 \cdot [\text{Fe}/\text{H}]^2 + \\ & \mathbf{a}_2 \cdot T_{\text{eff}} \cdot [\text{Fe}/\text{H}] + \\ & \mathbf{a}_3 \cdot T_{\text{eff}} + \mathbf{a}_4 \cdot [\text{Fe}/\text{H}] + \mathbf{a}_5, \end{aligned} \quad (1)$$

$$\mathbf{C}_0 = \mathbf{C} - \mathbf{R} \times E(G_{\text{BP}} - G_{\text{RP}}), \quad (2)$$

where

$$\mathbf{C} = \begin{pmatrix} G_{\text{BP}} - g \\ G_{\text{RP}} - r \\ G_{\text{RP}} - i \\ G_{\text{RP}} - z \\ G_{\text{RP}} - y \end{pmatrix}, \quad \mathbf{R} = \begin{pmatrix} R_{(G_{\text{BP}}-g)} \\ R_{(G_{\text{RP}}-r)} \\ R_{(G_{\text{RP}}-i)} \\ R_{(G_{\text{RP}}-z)} \\ R_{(G_{\text{RP}}-y)} \end{pmatrix}.$$

d. Moderate magnitude-dependent residuals are found when fitting intrinsic colors as a function of T_{eff} and $[\text{Fe}/\text{H}]$ of the control samples in each band. Therefore, we use a linear polynomial, $\Delta\mathbf{M}(\text{Mag}) = b_1 \cdot \mathbf{M}^{\text{obs}} + b_0$, to fit the residuals ($\mathbf{C}_0 - \mathbf{C}_0^{\text{mod}}(T_{\text{eff}}, [\text{Fe}/\text{H}])$). To account for magnitude-dependent errors in the PS1 data, corrected magnitudes are obtained by $\mathbf{M}^{\text{obs}} + \Delta\mathbf{M}(\text{Mag})$. Then, we put the corrected magnitudes into the previous step (Figure 1(c)). Iterations are performed.

e. Based on the results from the above two steps, intrinsic colors $\mathbf{C}_0^{\text{mod}}(T_{\text{eff}}, [\text{Fe}/\text{H}])$ are obtained for the calibration stars, so are their reddening values $\mathbf{C} - \mathbf{C}_0^{\text{mod}}$. Then, the reddening coefficients \mathbf{R} with respect to $E(G_{\text{BP}} - G_{\text{RP}})$ are derived by linear regression with 3σ clipping. Note that the lines are not forced to pass through the origin. The non-zero offsets, $\delta\mathbf{M}$, represent the zero-point differences between the control samples and the calibration samples. Iterations are also needed here, as shown in Figure 1. Finally, $\delta\mathbf{M} = (+0.0047, -0.0027, -0.0008, +0.0061, -0.0013)^{\text{T}}$ mag.

In this process, because of the very broad passbands of G_{BP} and G_{RP} , we have also considered the influence of temperature on the reddening coefficients. Temperature-dependent reddening coefficients are adopted for the $G_{\text{BP}} - g$ and $G_{\text{RP}} - r$ colors.

f. At last, the predicted model magnitudes \mathbf{M}^{mod} and magnitude offsets $\Delta\mathbf{M}(\text{RA}, \text{Dec})$ can be obtained from Equations (3) and (4):

$$\begin{aligned} \mathbf{M}^{\text{mod}} = & \mathbf{G}_{\text{BP,RP}} - \mathbf{C}_0^{\text{mod}}(T_{\text{eff}}, [\text{Fe}/\text{H}]) - \\ & \mathbf{R} \times E(G_{\text{BP}} - G_{\text{RP}}), \end{aligned} \quad (3)$$

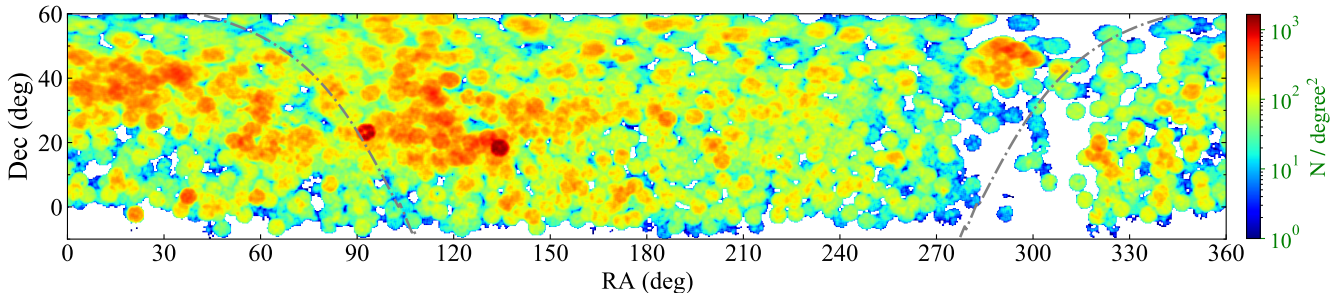


FIG. 3.— Spatial distribution of the calibration sample stars for the g band. A color bar is over-plotted to the right indicating the stellar number densities. The gray dotted line indicates the Galactic plane.

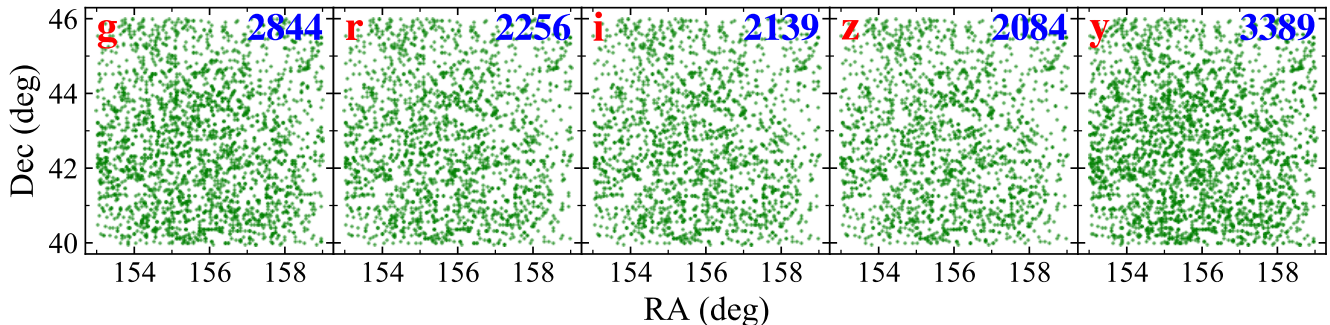


FIG. 4.— Spatial distributions of the control sample stars for the $grizy$ bands. The band and the star number are labeled in each panel.

$$\Delta\mathbf{M}(\text{RA}, \text{Dec}) = \mathbf{M}^{\text{mod}} - \mathbf{M}^{\text{obs}} - \delta\mathbf{M}. \quad (4)$$

4. RESULTS

The final fitting results of the intrinsic colors as a function of $(T_{\text{eff}}, [\text{Fe}/\text{H}])$ are shown in Figure 5. The corresponding fitting parameters are listed in Table 1. The fitting residuals are respectively 0.0097, 0.0080, 0.0067, 0.0067 and 0.0106 mag for the $G_{\text{BP}} - g$, $G_{\text{RP}} - r$, $G_{\text{RP}} - i$, $G_{\text{RP}} - y$ and $G_{\text{RP}} - z$ colors, suggesting that one can predict PS1 magnitudes to a precision of 1 per cent or better from the LAMOST and Gaia data for individual stars. The fitting residuals show no dependence on T_{eff} and $[\text{Fe}/\text{H}]$, and magnitude either after correcting the magnitude-dependent errors. The final fitting coefficients of magnitude-dependence corrections $\Delta\mathbf{M}(\text{Mag})$ are listed in Table 3. The slopes imply that magnitude-dependent corrections are 0.005, 0.005, 0.005, 0.004, 0.003 mag per magnitude in the 14 – 17 magnitude range for the $grizy$ bands, respectively. Note that the magnitude-dependent corrections are relative. The corrections are zero at $(g, r, i, z, y) = (15.1, 15.1, 15.2, 15.2, 14.3)$, which are the typical magnitudes of the control samples.

The results of reddening coefficients with respect to $E(G_{\text{BP}} - G_{\text{RP}})$ in the five colors are plotted in Figure 6. It can be seen that the reddening coefficients show moderate dependence on stellar temperature for the $G_{\text{BP}} - g$ and $G_{\text{RP}} - r$ colors. Therefore, taking 500 K as the bin width, the calibration stars are divided into 16 overlapping bins according to their temperature. Reddening coefficients of the 16 bins are further obtained via linear regression, with the same offset. Then, we use a cubic polynomial of 4 free parameters to fit the reddening

coefficients as a function of T_{eff} . The final fitting parameters are given in Table 2. The temperature dependence of reddening coefficients for the $G_{\text{RP}} - i$, $G_{\text{RP}} - y$ and $G_{\text{RP}} - z$ colors are very weak and ignored. Their fitting coefficients are given in Figure 6.

Figure 7 shows the spatial variations of magnitude offsets after binning with a $20' \times 20'$ window for the g , r , i , z and y bands. We can see both large-scale and small-scale patterns for all the five bands. The small-scale patterns, having a typical size similar to the PS1 field-of-view (3.3 degree), is more clearly displayed in Figure 8 for the i band. The same mottling also appears in Figure 10 of Magnier et al. (2020). The large-scale patterns are different between different bands. The y band shows the strongest patterns, probably due to the strong and variable water absorption of the atmosphere. The spatial patterns suggest that the magnitude offsets are caused by calibration errors in the PS1 rather than Gaia.

To investigate whether the derived magnitude offsets are affected by possible systematic errors in reddening correction, the correlations between the magnitude offsets of different bands are calculated and shown in Figure 9. The correlation coefficients are very close to zero, suggesting that systematic errors in reddening correction are very small. However, we note that the magnitude offsets of two bands can show clear correlations in certain sky areas.

To quantitatively estimate calibration errors of the PS1 data, we plot the magnitude offsets as a function of star numbers in one box in Figure 11. The standard deviations are also estimated using Gaussian fitting. The values decrease as the star numbers increases first, then become flat when the star numbers are larger than 10. The convergence values are respectively 4.6, 3.9, 3.5, 3.6, and 4.8 mmag for the g , r , i , z and y bands, confirming

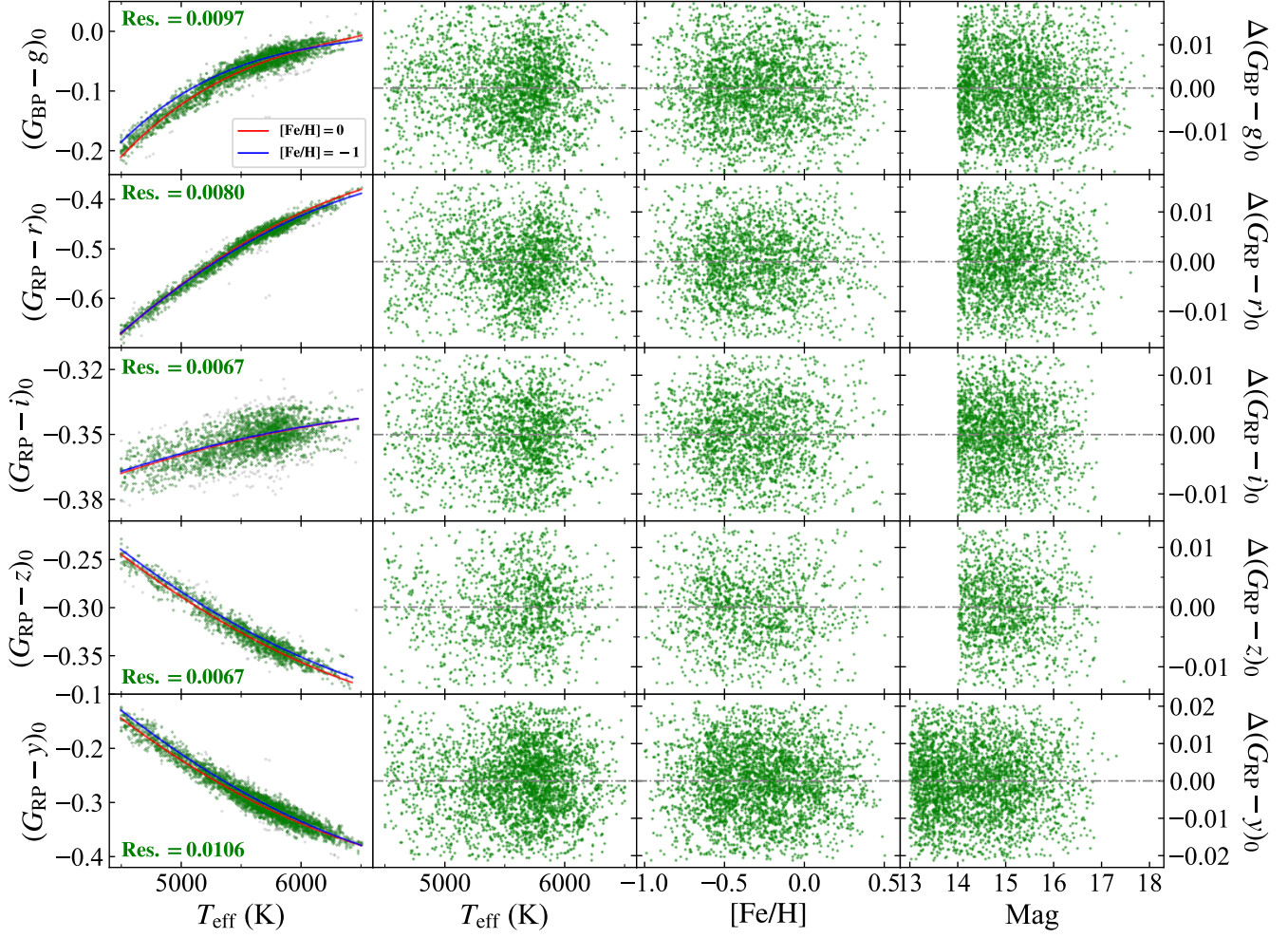


FIG. 5.— Two-dimensional 2-order polynomial fitting (with 6 free parameters) of intrinsic colors as functions of T_{eff} and $[\text{Fe}/\text{H}]$ for the control stars. From top to bottom are for the $G_{\text{BP}} - g$, $G_{\text{RP}} - r$, $G_{\text{RP}} - i$, $G_{\text{RP}} - z$ and $G_{\text{RP}} - y$ colors, respectively. The left column shows the fitting results after 3σ clipping, and the outliers are indicated by gray pluses. The red and blue curves represent results for $[\text{Fe}/\text{H}] = 0$ and -1 , respectively, and the fitting residuals are labeled. The 2nd, 3rd and 4th columns plot residuals against T_{eff} , $[\text{Fe}/\text{H}]$ and magnitude, respectively.

TABLE 1
THE COEFFICIENTS USED TO OBTAIN INTRINSIC COLORS AS FUNCTIONS OF T_{eff} AND $[\text{Fe}/\text{H}]$ IN THE FIVE BANDS.

Intrinsic Color	T_{eff}^2	$[\text{Fe}/\text{H}]^2$	$T_{\text{eff}} \cdot [\text{Fe}/\text{H}]$	T_{eff}	$[\text{Fe}/\text{H}]$	Constant Term
$(G_{\text{BP}} - g)_0$	-4.520×10^{-8}	-5.120×10^{-3}	1.723×10^{-5}	5.892×10^{-4}	-1.097×10^{-1}	-1.940
$(G_{\text{RP}} - r)_0$	-3.407×10^{-8}	4.415×10^{-3}	4.052×10^{-6}	5.192×10^{-4}	-1.456×10^{-2}	-2.317
$(G_{\text{RP}} - i)_0$	-2.742×10^{-9}	3.609×10^{-3}	5.390×10^{-7}	4.278×10^{-5}	7.821×10^{-5}	-0.505
$(G_{\text{RP}} - z)_0$	1.314×10^{-8}	1.310×10^{-3}	-3.992×10^{-7}	-2.124×10^{-4}	-1.899×10^{-3}	0.444
$(G_{\text{RP}} - y)_0$	2.462×10^{-8}	-5.528×10^{-3}	7.085×10^{-6}	-3.881×10^{-4}	-5.183×10^{-2}	1.104

that the PS1 data has achieved an internal precision of $< 1\%$ mag (Schlafly et al. 2012).

To correct the above patterns, we perform an adaptive median smoothing. The initial box size is $20' \times 20'$. If the star numbers within a box is less than 20, then the box size is doubled until it reaches to $160'$. The results of the five bands after smoothing are plotted in Figure 10, and can be used to correct calibration errors in the PS1 data within the LAMOST footprint. The data is publicly available². The corrected magnitude M^{corr} can be

computed as

$$M^{\text{corr}} = M^{\text{obs}} + \Delta M(\text{RA}, \text{Dec}) + \Delta M(\text{Mag}), \quad (5)$$

where M^{obs} is the observed magnitude, $\Delta M(\text{RA}, \text{Dec})$ is the position-dependent magnitude offset (see Figure 10), and $\Delta M(\text{Mag})$ is the magnitude-dependent magnitude offset (see Table 3). To check the effect of correction, we over-plot the magnitude offsets after correction as a function of star numbers in Figure 11. The standard deviations decrease to 0.4 – 0.5 mmag for the five bands.

² http://paperdata.china-vo.org/Xiao.Kai/PS1/spatial_

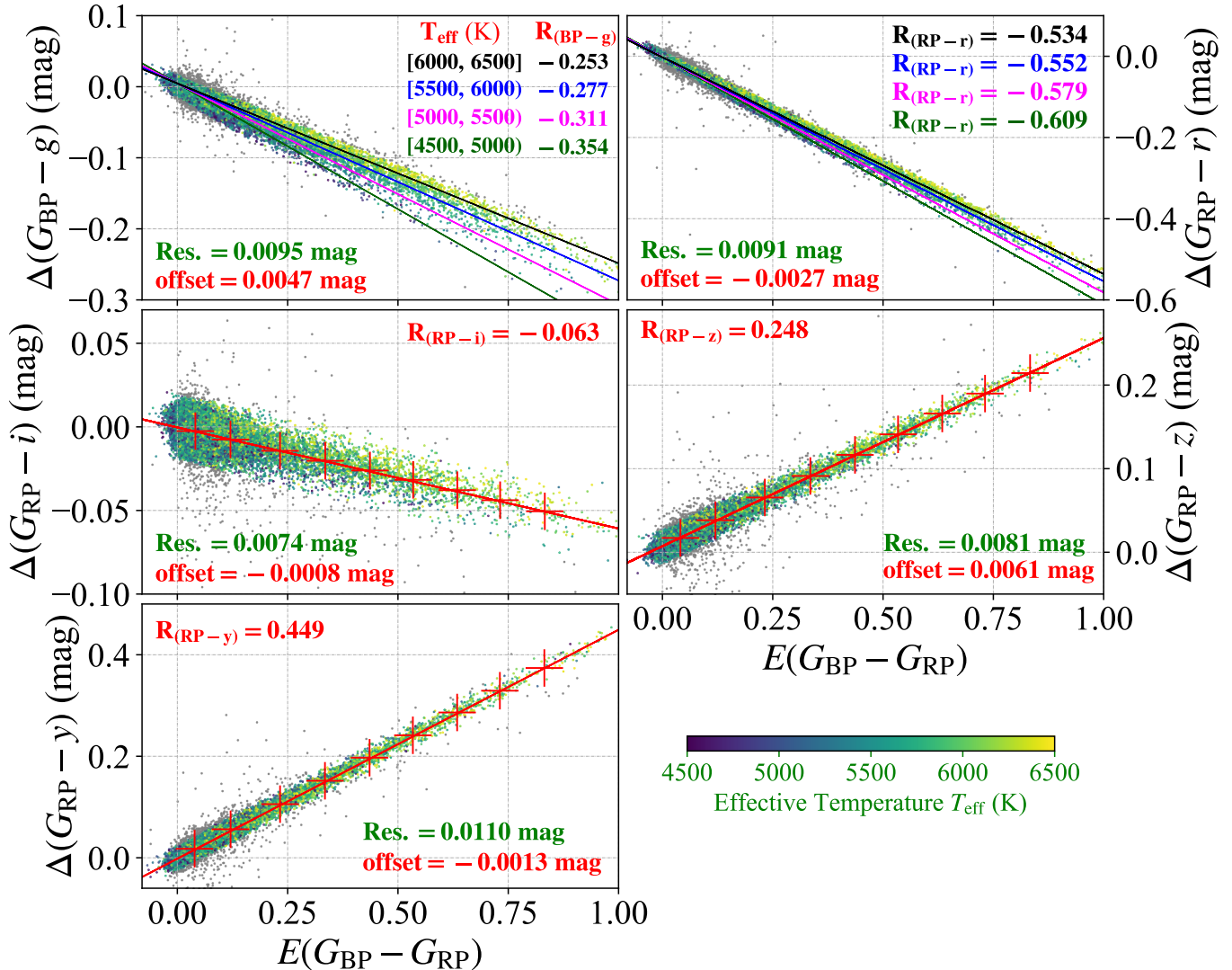


FIG. 6.— Linear regression of reddening coefficients of the $G_{\text{BP}} - g$, $G_{\text{RP}} - r$, $G_{\text{RP}} - i$, $G_{\text{RP}} - z$ and $G_{\text{RP}} - y$ colors with respect to $E(G_{\text{BP}} - G_{\text{RP}})$ for the calibration samples. To avoid crowding, only one in fifty stars are plotted. Colors indicate different temperatures. For the middle and bottom panels where reddening coefficients show weak dependence on temperature, the red pluses are the median values after 3σ clipping and the outliers are indicated by gray pluses; the red lines are linear fits to the red pluses; the slopes, offsets, and fitting residuals are all labeled. For the two top panels where reddening coefficients show moderate temperature dependence, the fitted reddening coefficients for four temperature ranges are shown.

TABLE 2
TEMPERATURE-DEPENDENT REDDENING COEFFICIENTS OF $G_{\text{BP}} - g$ AND $G_{\text{RP}} - r$ WITH RESPECT TO $E(G_{\text{BP}} - G_{\text{RP}})$.

Color	T_{eff}^3	T_{eff}^2	T_{eff}	Constant
$G_{\text{BP}} - g$	-1.765×10^{-12}	1.094×10^{-8}	1.080×10^{-4}	-0.925
$G_{\text{RP}} - r$	-1.434×10^{-11}	2.183×10^{-7}	-1.041×10^{-3}	0.941

We also apply our corrected magnitudes of PS1 back to the linear regression process of reddening coefficients. All the fitting residuals are smaller, decreasing from 9.5 to 8.3, 9.1 to 8.2, 7.4 to 6.8, 8.1 to 7.3, and 11.0 to 9.5 mmag for the *grizy* bands, respectively. These numbers are consistent with those in Figure 11. For example, $\sqrt{9.5^2 - 8.3^2} \sim 4.6$.

5. DISCUSSIONS

After correcting for the magnitude-dependent errors, we plot variation of magnitude offsets with magnitudes and $G_{\text{BP}} - G_{\text{RP}}$ color of the calibration samples in Figure 12. As expected, no dependence on magnitudes is found. The dependence on $G_{\text{BP}} - G_{\text{RP}}$ is also ignorable.

To further verify the magnitude-dependent corrections, we perform an independent check using data from the recalibrated SDSS Stripe 82 standard stars catalog (V4.2; Huang & Yuan 2022) and DES DR1. Stars within a sub-

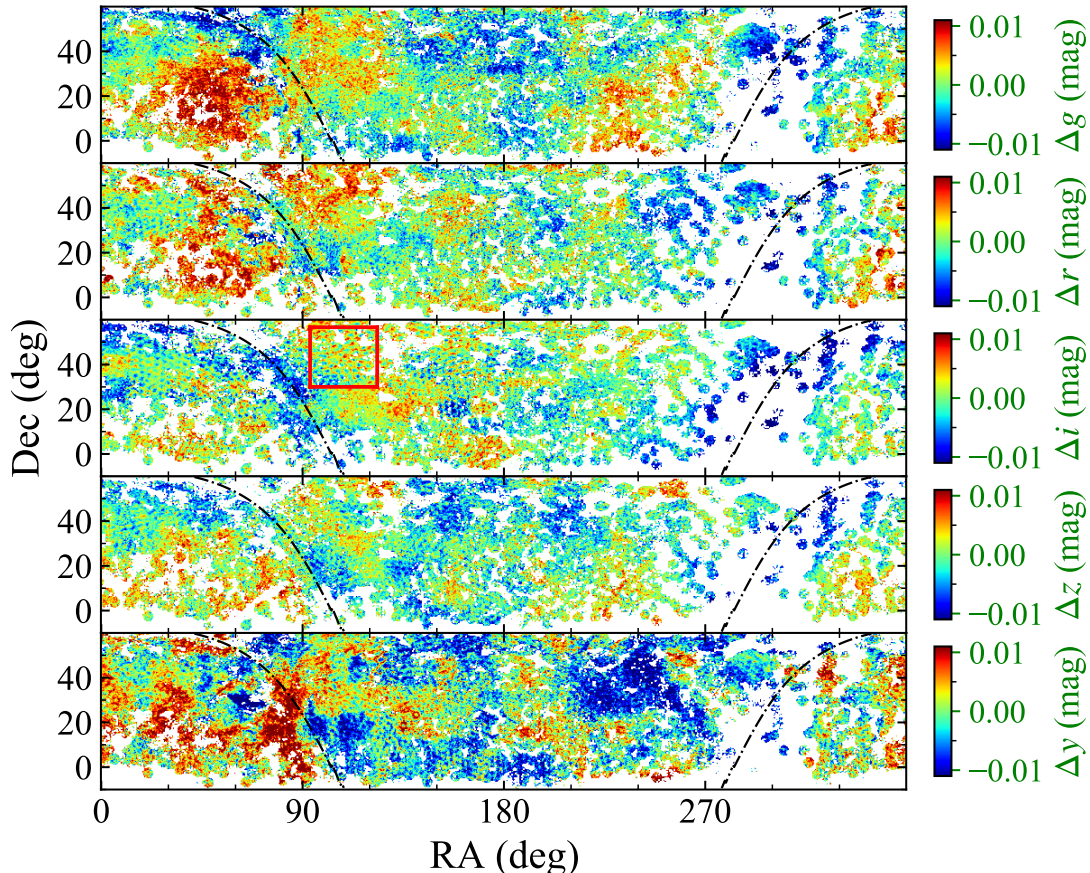


FIG. 7.— Spatial variations of magnitude offsets after a $20' \times 20'$ binning in the g , r , i , z and y bands. The black dotted line indicates the Galactic plane in each panel. Color bars are over-plotted to the right. The small region marked with a red box in the i band is re-plotted in Figure 8.

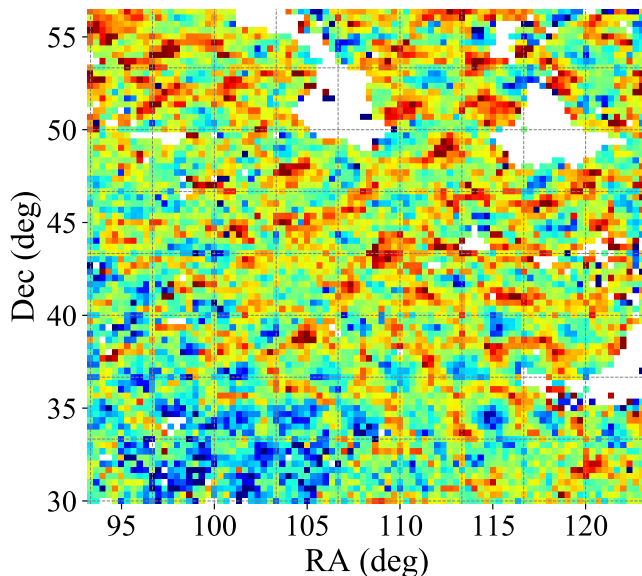


FIG. 8.— A zoom in plot for the small region in Figure 7 (red box) in the i band with the same color bar. The spacing of the gray grids is 3.3° .

stripe of $|\text{Dec}| < 1.266^\circ$ and $23^{\text{h}}00^{\text{m}} < \text{RA} < 2^{\text{h}}40^{\text{m}}$ are used. All these stars are in the high Galactic latitude region and suffer very low extinction. First, we construct different color-color relations, e.g., $r_{\text{SDSS}} - r$

TABLE 3
THE COEFFICIENTS USED FOR
MAGNITUDE-DEPENDENT CORRECTIONS.

$\Delta\mathbf{M}$ (Mag)	Slope (b_1)	Constant (b_0)
Δg	0.0050	-0.0755
Δr	0.0048	-0.0727
Δi	0.0045	-0.0686
Δz	0.0038	-0.0576
Δy	0.0029	-0.0415

versus $g_{\text{SDSS}} - i_{\text{SDSS}}$, and use them to obtain the predicted PS1 magnitudes from the SDSS/DES magnitudes and colors. Note that the filter differences between different surveys are corrected here via color-color relations. Then we plot the offsets between the predicted and observed PS1 magnitudes as a function of PS1 magnitude. An example of the magnitude offset in r band from the SDSS Stripe 82 varying with r is shown in Figure 13. The results are summarized in Figure 14. Note that the results from the SDSS and DES are shifted slightly in the vertical direction for easy comparison.

Figure 14 shows that for the g , r , and i bands, both the results of SDSS stripe 82 and DES DR1 agree well with our corrections from Gaia EDR3 for magnitudes between 14 – 17. For the z band, our corrections are consistent with those of DES DR1 only. For the y band, only result from the DES DR1 is obtained, with a much deeper slope. The results suggest that the moderate magnitude-

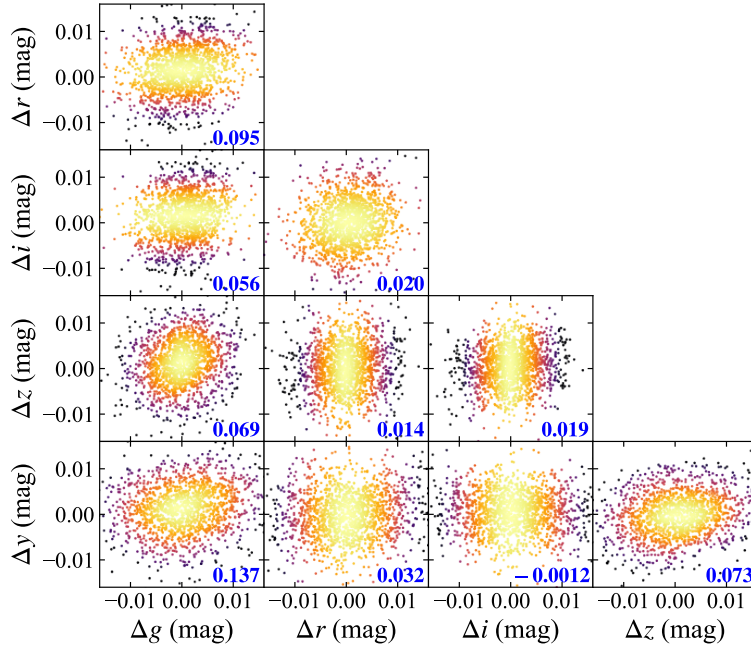


FIG. 9.— The correlation plots between the magnitude offsets with a restriction of the star numbers of box is more than 5 for each two bands. For each panel, the correlation coefficient are marked. The color in each panel indicates number density of stars.

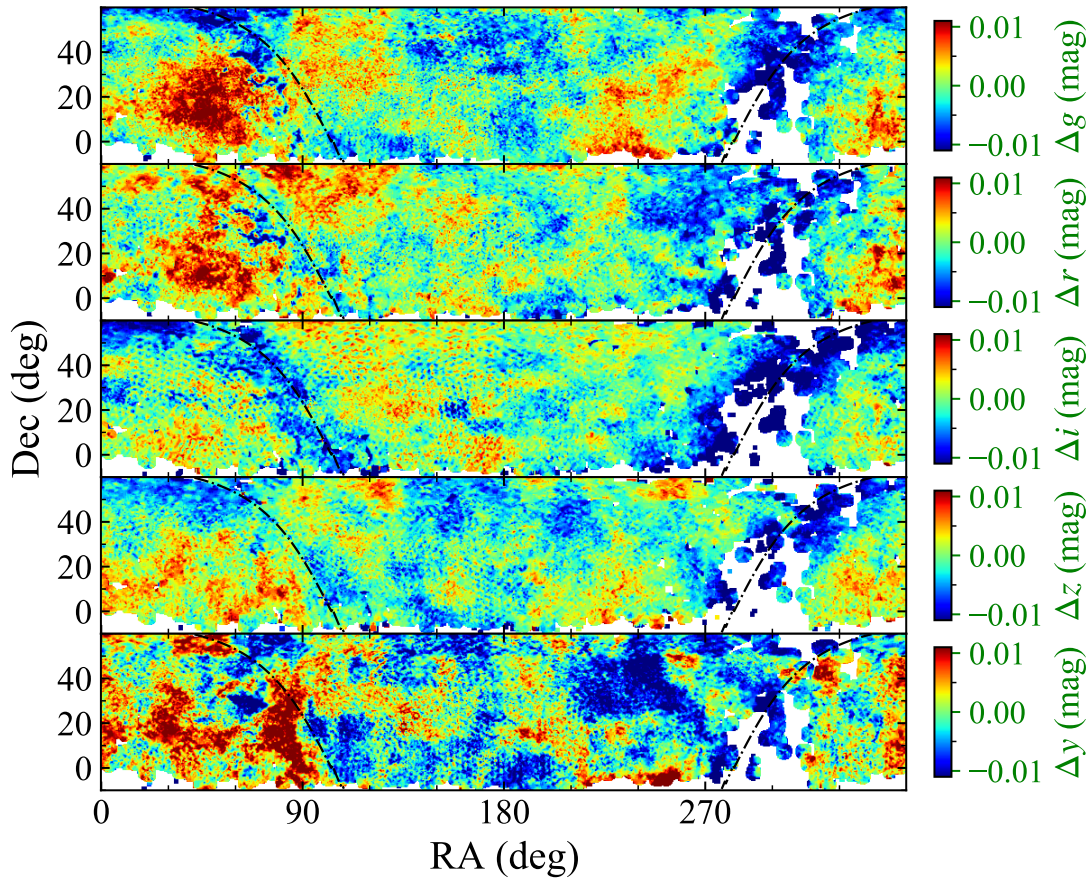


FIG. 10.— Same to Figure 7 but after smoothing.

dependent errors in the PS1 magnitudes are real.

To investigate the possible causes of the magnitude-dependent errors, we select 20,000 stars from PS1 DR1

and compare their aperture-based and PSF magnitudes. Note that all the magnitudes mentioned earlier refer to the PSF magnitudes in this work. The results are plotted

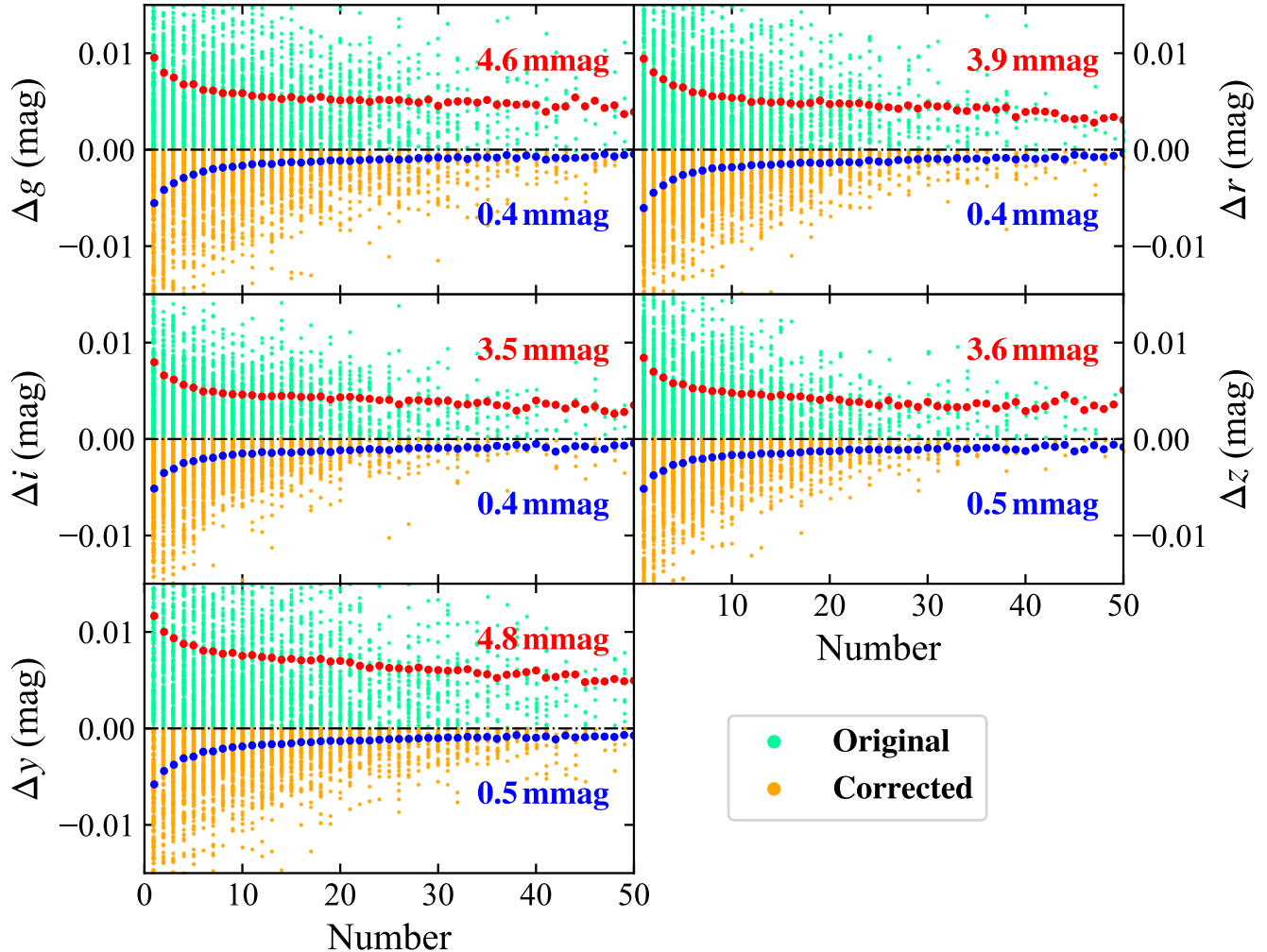


FIG. 11.— Magnitude offsets as a function of star numbers in $20' \times 20'$ region before and after correction. From top to bottom are for the g , r , i , z and y bands, respectively. The green (orange) pluses are the initial (corrected) magnitude offsets, and their standard deviations are indicated by red (blue) dots. The convergence value of the scatter is marked in each panel.

in Figure 15. These results are also plotted in Figure 14 with green dots for comparison, after shifting of the zero points. Figure 14 suggests that our corrections from Gaia EDR3 agree with the differences between the aperture-based and PSF magnitudes in each band. It implies that most of the magnitude-dependent errors in the PS1 PSF magnitudes probably come from systematic errors in the PSF magnitudes. Note that the uncertainties in the non-linearity corrections of the CCDs may also contribute partly.

Portillo et al. (2020) noted that the PSF photometry using maximum-likelihood methods systematically overestimate the flux, with a bias scaling with the inverse signal-to-noise ratio and the number of model parameters involved in the fit. One expects a 1 per cent bias for a 10σ point source and 0.01 per cent bias for a 100σ point source. Given the brightness of the calibration stars used in this work, such effect may contribute only a small fraction to the systematic errors in the PS1 PSF magnitudes.

6. CONCLUSIONS

In this paper, using the SCR method with the photometric data from the corrected Gaia EDR3 and the

spectroscopic data from LAMOST DR7, we have performed an independent validation and recalibration of the PS1 photometry. Using typically a total of 1.5 million LAMOST-PS1-Gaia FGK dwarf stars as standards per band, we show that the PS1 photometric calibration precisions are respectively 4.6, 3.9, 3.5, 3.6, and 4.8 mmag in the $grizy$ bands when averaged over $20'$ regions. However, significant large- and small-scale spatial variation of magnitude offsets, up to over 1 per cent and caused by calibration errors in the PS1, are found for all the $grizy$ filters. The calibration errors in different filters are un-correlated in most sky areas. The y band shows the strongest patterns, probably due to the strong and variable water absorption of the atmosphere.

We also detect the moderate magnitude-dependent errors in the PS1 photometry, i.e., 0.005, 0.005, 0.005, 0.004, 0.003 mag per magnitude in the 14 – 17 magnitude range for the $grizy$ filters, respectively. Such errors are further confirmed by comparing the PS1 magnitudes with those predicted from the re-calibrated SDSS Stripe 82 standard stars catalog (V4.2) and DES DR1. Such errors are likely caused by systematic uncertainties in the PSF magnitudes.

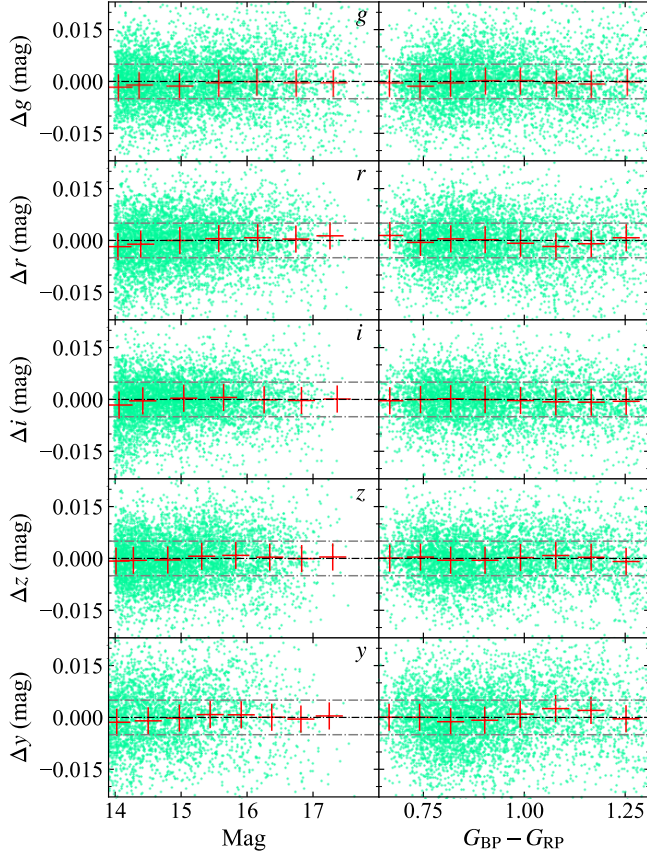


FIG. 12.— The variations of magnitude offset as a function of magnitude (left) and $G_{BP} - G_{RP}$ (right) in g , r , i , z and y bands. The red pluses are the median values. The black and gray dotted lines in each panel denote magnitude offsets of 0 and ± 5 mmag, respectively.

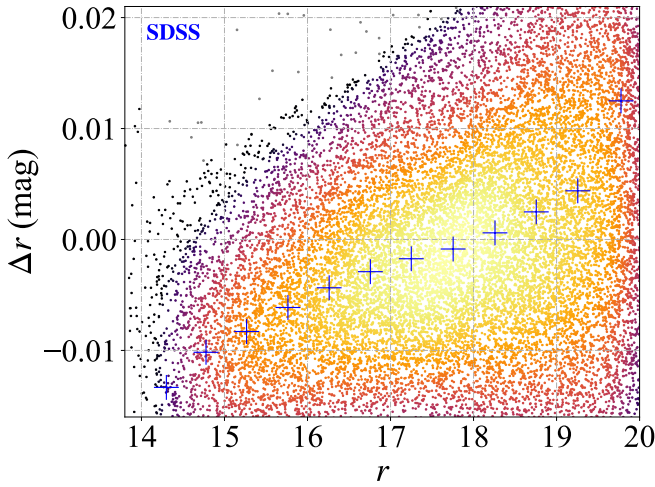


FIG. 13.— An example showing the variations of r magnitude offset as a function of r magnitude obtained by comparing with the SDSS stripe 82 data. The blue pluses are the median values. The color represents the number density of stars.

It implies that most of the magnitude-dependent errors in the PS1 PSF magnitudes probably come from systematic errors in the PSF magnitudes. Note that the uncertainties in the non-linearity corrections of the CCDs may also contribute partly.

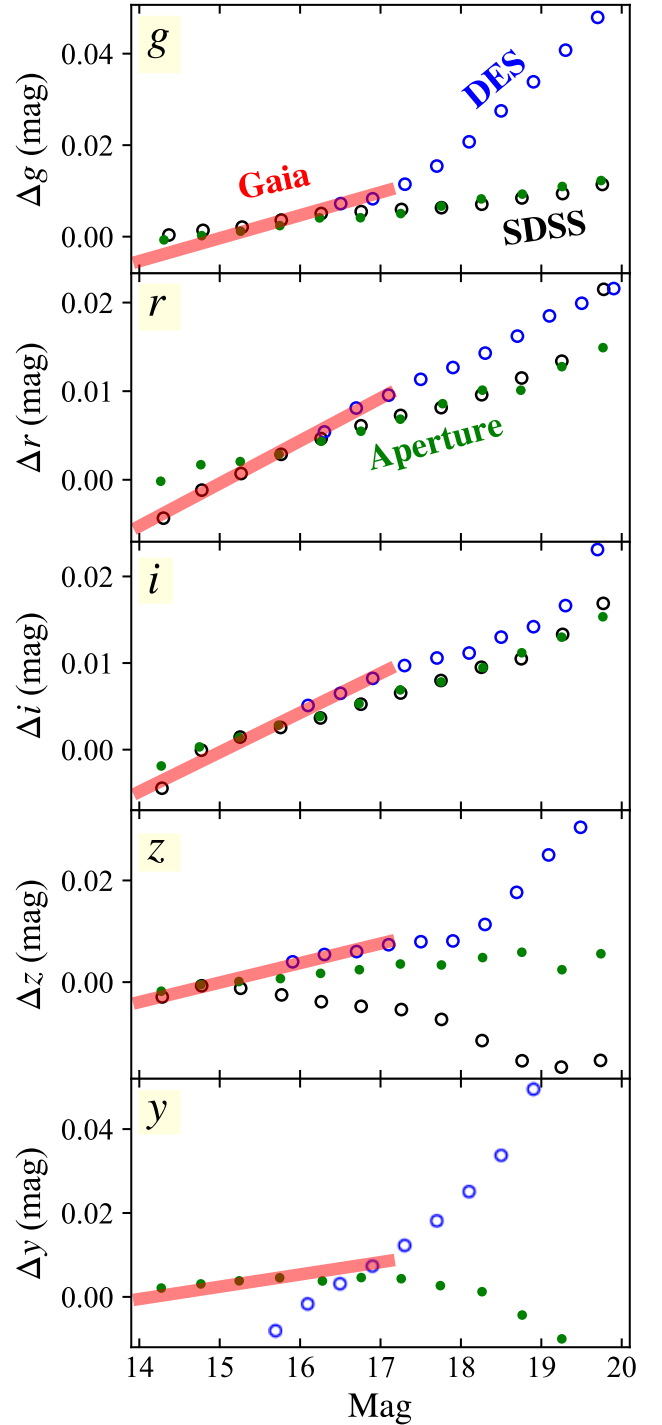


FIG. 14.— The variations of magnitude offset as a function of magnitude in the five bands. The black and blue circles denote results from the SDSS Stripe 82 and DES DR1, respectively. The green dots denote results of comparison with the aperture-based magnitudes of PS1. The red lines denote results from Gaia.

We provide two-dimensional maps to correct for position-dependent magnitude offsets in the LAMOST footprint at resolutions from $20'$ to $160'$. The maps, together with the magnitude-dependent corrections, are useful in the usage of the PS1 photometry for high-precision investigations (e.g., Niu et al. 2021c; Xu et al.

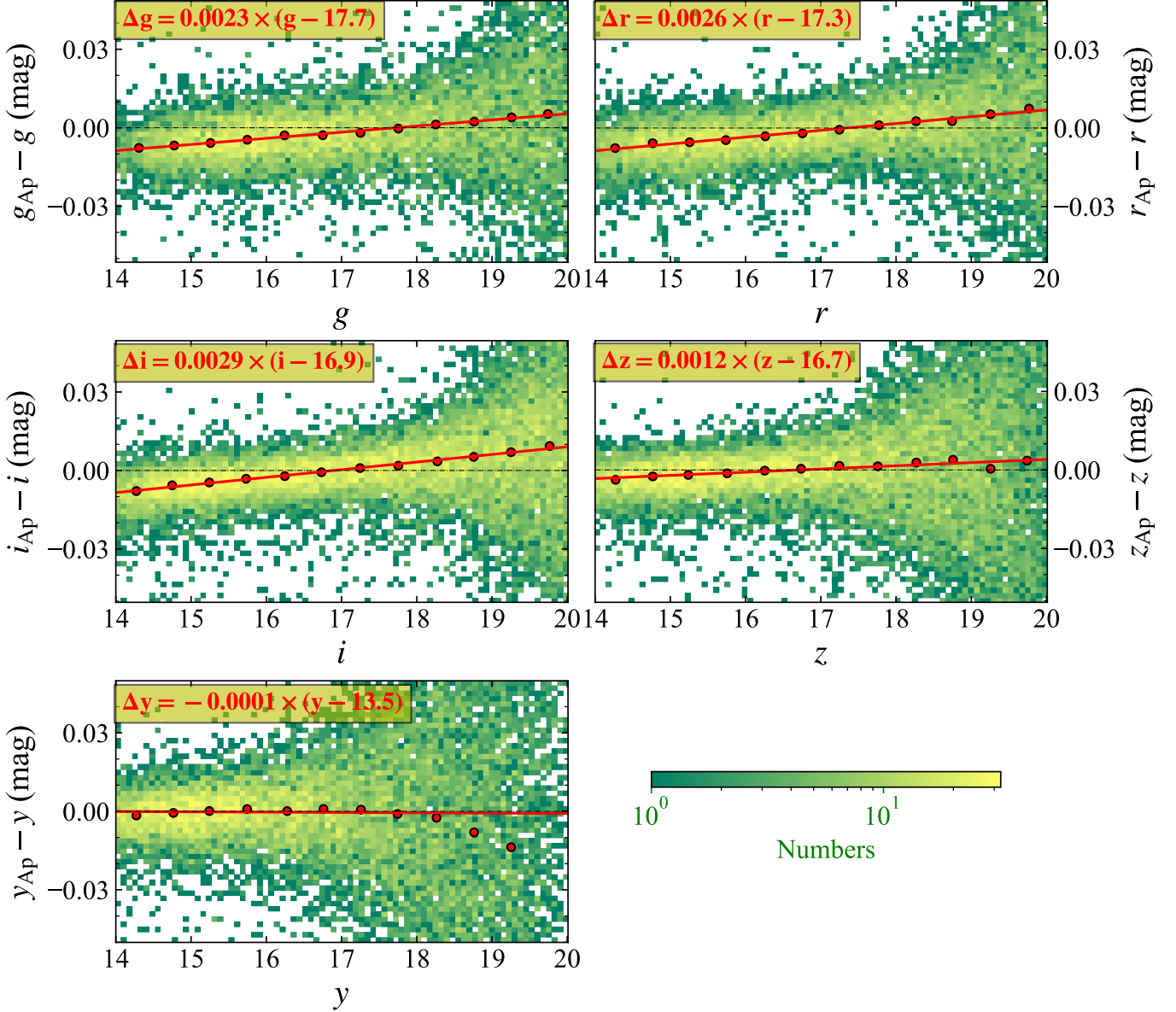


FIG. 15.— The difference between the aperture-based and PSF magnitudes as a function of PSF magnitude in the five bands. The black points in each panel are the median values. The linear fitting results to these dots are over-plotted in red lines and marked.

2021) and as the reference to calibrate other surveys.

The results demonstrate the power of the SCR method in improving calibration precision of wide-field surveys when combined with Gaia photometry. We suggest that the SCR method should be incorporated into the calibration process of future releases of the PS1 data.

We thank Prof. Xiaowei Liu for valuable discussions and a careful reading of the manuscript. This work is supported by the National Natural Science Foundation of China through the project NSFC 12173007 and 11603002, the National Key Basic R&D Program of China via 2019YFA0405503 and Beijing Normal University grant No. 310232102. We acknowledge the science research grants from the China Manned Space Project with NO. CMS-CSST-2021-A08 and CMS-CSST-2021-A09.

This work has made use of data from the European Space Agency (ESA) mission Gaia (<https://www.cosmos.esa.int/gaia>), processed by the Gaia Data Processing and Analysis Consortium (DPAC, <https://www.cosmos.esa.int/web/gaia/dpac/consortium>). Funding for the DPAC has been provided by national institutions, in particular the institutions participating in the Gaia Multilateral Agreement. Guoshoujing Telescope (the Large Sky Area Multi-Object Fiber Spectroscopic Telescope LAMOST) is a National Major Scientific Project built by the Chinese Academy of Sciences. Funding for the project has been provided by the National Development and Reform Commission. LAMOST is operated and managed by the National Astronomical Observatories, Chinese Academy of Sciences.

The Pan-STARRS1 Surveys (PS1) and the PS1 public

science archive have been made possible through contributions by the Institute for Astronomy, the University of Hawaii, the Pan-STARRS Project Office, the Max-Planck Society and its participating institutes, the Max Planck Institute for Astronomy, Heidelberg and the Max Planck Institute for Extraterrestrial Physics, Garching, The Johns Hopkins University, Durham University, the University of Edinburgh, the Queen's University Belfast, the Harvard-Smithsonian Center for Astrophysics, the Las Cumbres Observatory Global Tele-

scope Network Incorporated, the National Central University of Taiwan, the Space Telescope Science Institute, the National Aeronautics and Space Administration under Grant No. NNX08AR22G issued through the Planetary Science Division of the NASA Science Mission Directorate, the National Science Foundation Grant No. AST-1238877, the University of Maryland, Eotvos Lorand University (ELTE), the Los Alamos National Laboratory, and the Gordon and Betty Moore Foundation.

REFERENCES

- Abbott, T. M. C., Abdalla, F. B., Allam, S., et al. 2018, *ApJS*, 239, 18. doi:10.3847/1538-4365/aae9f0
- Benitez, N., Dupke, R., Moles, M., et al. 2014, arXiv:1403.5237
- Brout, D., Taylor, G., Scolnic, D., et al. 2021, arXiv:2112.03864
- Burke, D. L., Rykoff, E. S., Allam, S., et al. 2018, *AJ*, 155, 41. doi:10.3847/1538-3881/aa9f22
- Chambers, K. C., Magnier, E. A., Metcalfe, N., et al. 2016, arXiv:1612.05560
- Cui, X.-Q., Zhao, Y.-H., Chu, Y.-Q., et al. 2012, *Research in Astronomy and Astrophysics*, 12, 1197. doi:10.1088/1674-4527/12/9/003
- Dark Energy Survey Collaboration, Abbott, T., Abdalla, F. B., et al. 2016, *MNRAS*, 460, 1270. doi:10.1093/mnras/stw641
- Deng, L.-C., Newberg, H. J., Liu, C., et al. 2012, *Research in Astronomy and Astrophysics*, 12, 735. doi:10.1088/1674-4527/12/7/003
- Finkbeiner, D. P., Schlafly, E. F., Schlegel, D. J., et al. 2016, *ApJ*, 822, 66. doi:10.3847/0004-637X/822/2/66
- Flaugher, B., Diehl, H. T., Honscheid, K., et al. 2015, *AJ*, 150, 150. doi:10.1088/0004-6256/150/5/150
- Gaia Collaboration, Prusti, T., de Bruijne, J. H. J., et al. 2016, *A&A*, 595, A1. doi:10.1051/0004-6361/201629272
- Gaia Collaboration, Brown, A. G. A., Vallenari, A., et al. 2021a, *A&A*, 649, A1. doi:10.1051/0004-6361/202039657
- Gaia Collaboration, Brown, A. G. A., Vallenari, A., et al. 2021b, *A&A*, 650, C3. doi:10.1051/0004-6361/202039657e
- High, F. W., Stubbs, C. W., Rest, A., et al. 2009, *AJ*, 138, 110. doi:10.1088/0004-6256/138/1/110
- Huang, B. & Yuan, H. 2022, *ApJS*, in press
- Huang, Y., Beers, T. C., Wolf, C., et al. 2021, arXiv:2104.14154
- Huang, Y., Yuan, H., Li, C., et al. 2021, *ApJ*, 907, 68. doi:10.3847/1538-4357/abca37
- Hodapp, K. W., Kaiser, N., Aussel, H., et al. 2004, *Astronomische Nachrichten*, 325, 636. doi:10.1002/asna.200410300
- Ivezić, Ž., Smith, J. A., Miknaitis, G., et al. 2007, *AJ*, 134, 973. doi:10.1086/519976
- Ivezić, Ž., Kahn, S. M., Tyson, J. A., et al. 2019, *ApJ*, 873, 111. doi:10.3847/1538-4357/ab042c
- Kaiser, N., Aussel, H., Burke, B. E., et al. 2002, *Proc. SPIE*, 4836, 154. doi:10.1117/12.457365
- Kaiser, N., Burgett, W., Chambers, K., et al. 2010, *Proc. SPIE*, 7733, 77330E. doi:10.1117/12.859188
- Lee, Y. S., Beers, T. C., Sivarani, T., et al. 2008a, *AJ*, 136, 2022. doi:10.1088/0004-6256/136/5/2022
- Lee, Y. S., Beers, T. C., Sivarani, T., et al. 2008b, *AJ*, 136, 2050. doi:10.1088/0004-6256/136/5/2050
- Liu, X.-W., Yuan, H.-B., Huo, Z.-Y., et al. 2014, *Setting the scene for Gaia and LAMOST*, 298, 310. doi:10.1017/S1743921313006510
- Lou, Z., Liang, M., Yao, D., et al. 2016, *Proc. SPIE*, 10154, 101542A. doi:10.1117/12.2248371
- López-Sanjuan, C., Varela, J., Cristóbal-Hornillos, D., et al. 2019, *A&A*, 631, A119. doi:10.1051/0004-6361/201936405
- López-Sanjuan, C., Yuan, H., Vázquez Ramió, H., et al. 2021, *A&A*, 654, A61. doi:10.1051/0004-6361/202140444
- Luo, A.-L., Zhao, Y.-H., Zhao, G., et al. 2015, *Research in Astronomy and Astrophysics*, 15, 1095. doi:10.1088/1674-4527/15/8/002
- Magnier, E. A., Schlafly, E. F., Finkbeiner, D. P., et al. 2020, *ApJS*, 251, 6. doi:10.3847/1538-4365/abb82a
- Niu, Z., Yuan, H., & Liu, J. 2021a, *ApJ*, 909, 48. doi:10.3847/1538-4357/abdbac
- Niu, Z., Yuan, H., & Liu, J. 2021b, *ApJ*, 908, L14. doi:10.3847/2041-8213/abe1c2
- Niu, Z., Yuan, H., Wang, S., et al. 2021c, *ApJ*, 922, 211. doi:10.3847/1538-4357/ac2573
- Padmanabhan, N., Schlegel, D. J., Finkbeiner, D. P., et al. 2008, *ApJ*, 674, 1217. doi:10.1086/524677
- Portillo, S. K. N., Speagle, J. S., & Finkbeiner, D. P. 2020, *AJ*, 159, 165. doi:10.3847/1538-3881/ab76ba
- Riello, M., De Angeli, F., Evans, D. W., et al. 2021, *A&A*, 649, A3. doi:10.1051/0004-6361/202039587
- Ruoyi, Z. & Haibo, Y. 2020, *ApJ*, 905, L20. doi:10.3847/2041-8213/abccc4
- Schlafly, E. F., Finkbeiner, D. P., Jurić, M., et al. 2012, *ApJ*, 756, 158. doi:10.1088/0004-637X/756/2/158
- Schlegel, D. J., Finkbeiner, D. P., & Davis, M. 1998, *ApJ*, 500, 525. doi:10.1086/305772
- Scolnic, D., Casertano, S., Riess, A., et al. 2015, *ApJ*, 815, 117. doi:10.1088/0004-637X/815/2/117
- Thanjavur, K., Ivezić, Ž., Allam, S. S., et al. 2021, *MNRAS*, 505, 5941. doi:10.1093/mnras/stab1452
- Tonry, J. L., Stubbs, C. W., Lykke, K. R., et al. 2012, *ApJ*, 750, 99. doi:10.1088/0004-637X/750/2/99
- Wolf, C., Onken, C. A., Luvaul, L. C., et al. 2018, *PASA*, 35, e010. doi:10.1017/pasa.2018.5
- Wu, Y., Luo, A.-L., Li, H.-N., et al. 2011, *Research in Astronomy and Astrophysics*, 11, 924. doi:10.1088/1674-4527/11/8/006
- Xiang, M. S., Liu, X. W., Yuan, H. B., et al. 2015, *MNRAS*, 448, 822. doi:10.1093/mnras/stu2692
- Xiang, M.-S., Liu, X.-W., Shi, J.-R., et al. 2017, *MNRAS*, 464, 3657. doi:10.1093/mnras/stw2523
- Xu, S., Yuan, H., Niu, Z., et al. 2021, arXiv:2111.11725
- Yang, L., Yuan, H., Zhang, R., et al. 2021, *ApJ*, 908, L24. doi:10.3847/2041-8213/abdbae
- York, D. G., Adelman, J., Anderson, J. E., et al. 2000, *AJ*, 120, 1579. doi:10.1086/301513
- Yuan, H. B., Liu, X. W., & Xiang, M. S. 2013, *MNRAS*, 430, 2188. doi:10.1093/mnras/stt039
- Yuan, H., Liu, X., Xiang, M., et al. 2015, *ApJ*, 799, 133. doi:10.1088/0004-637X/799/2/133
- Zhan, H. 2018, 42nd COSPAR Scientific Assembly, 42, E1.16-4-18
- Zhao, G., Zhao, Y.-H., Chu, Y.-Q., et al. 2012, *Research in Astronomy and Astrophysics*, 12, 723. doi:10.1088/1674-4527/12/7/002
- Zhou, Z., Zhou, X., Zou, H., et al. 2018, *PASP*, 130, 085001. doi:10.1088/1538-3873/aaca7e
- Zou, H., Zhang, T., Zhou, Z., et al. 2017, *AJ*, 153, 276. doi:10.3847/1538-3881/aa72d9